Acta Oceanol. Sin., 2021, Vol. 40, No. 7, P. 42–57
https://doi.org/10.1007/s13131-021-1814-2
http://www.aosocean.com
E-mail: ocean2@hyxb.org.cn

Characteristics of oceanic mesoscale variabilities associated with the inverse kinetic energy cascade

Mengmeng Li[1, 2], Zhiliang Liu[3, 4*], Jianing Li[5, 6], Chongguang Pang[1, 6]

[1] Key Laboratory of Ocean Circulation and Waves, Institute of Oceanology, Chinese Academy of Sciences, Qingdao 266071, China

[2] University of Chinese Academy of Sciences, Beijing 100049, China

[3] Research Center for Marine Science, Hebei Normal University of Science and Technology, Qinhuangdao 066004, China

[4] Hebei Key Laboratory of Ocean Dynamics, Resources and Environments, Hebei Normal University of Science and Technology, Qinhuangdao 066004, China

[5] Physical Oceanography Laboratory, Ocean University of China, Qingdao 266100, China

[6] Pilot National Laboratory for Marine Science and Technology (Qingdao), Qingdao 266237, China

Received 6 October 2020; accepted 9 January 2021

Abstract

Oceanic geostrophic turbulence theory predicts significant inverse kinetic energy (KE) cascades at scales larger than the energy injection wavelength. However, the characteristics of the mesoscale variabilities associated with the inverse KE cascade in the real oceans have not been clear enough up to now. To further examine this problem, we analyzed the spectral characteristics of the oceanic mesoscale motions over the scales of inverse KE cascades based on high-resolution gridded altimeter data. The applicability of the quasigeostrophic (QG) turbulence theory and the surface quasigeostrophic (SQG) turbulence theory in real oceans is further explored. The results show that the sea surface height (SSH) spectral slope is linearly related to the eddy-kinetic-energy (EKE) level with a high correlation coefficient value of 0.67. The findings also suggest that the QG turbulence theory is an appropriate dynamic framework at the edge of high-EKE regions and that the SQG theory is more suitable in tropical regions and low-EKE regions at mid-high latitudes. New anisotropic characteristics of the inverse KE cascade are also provided. These results indicate that the along-track spectrum used by previous studies cannot reveal the dynamics of the mesoscale variabilities well.

Key words: mesoscale eddy, inverse cascade, scalar wavenumber spectrum, spectral slope, anisotropy

Citation: Li Mengmeng, Liu Zhiliang, Li Jianing, Pang Chongguang. 2021. Characteristics of oceanic mesoscale variabilities associated with the inverse kinetic energy cascade. Acta Oceanologica Sinica, 40(7): 42–57, doi: 10.1007/s13131-021-1814-2

1 Introduction

Energy balance in ocean dynamics, in which ocean eddies play a key role, is crucial to predicting the state of ocean circulation and its evolution. To date, the generation mechanism and the balance process of eddies are still unclear. As predicted by the linear baroclinic instability theory, mesoscale eddies generate and obtain energy mainly from time-mean flows at the deformation scale, L_r (Ferrari and Wunsch, 2009; Kobashi and Kawamura, 2002; Wang et al., 2015; Salmon, 1998). However, the observed energy-containing scales inferred from diagnoses of spectral energy fluxes are approximately 100 km larger than that predicted by the linear theory (Smith, 2007). The inverse kinetic energy (KE) cascade process may be a bridge connecting this gap (Smith, 2007; Wang et al., 2015).

As is well known, two-dimensional (2-D) turbulence predicts two inertial ranges of energy spectra: an energy inertial range carrying KE from L_r to larger scales (inverse cascade) and an enstrophy inertial range carrying enstrophy to smaller scales (forward cascade) (Kraichnan, 1967; Vallis, 2007). After generating at L_r, most mesoscale eddies will grow through the inverse KE cascade process due to nonlinear triad interactions (Stewart et al., 1996; Scott and Wang, 2005; Kobashi and Kawamura, 2002) and equilibrate at some halting scale, L_equ (Vallis, 2007). The features observed by satellites should be around the scales of eddy equilibration near L_equ. Thus, inverse KE cascade within the scales of $L_\mathrm{r} < L < L_\mathrm{equ}$ is important for understanding how mesoscale eddies interact among themselves and to what extent this interaction contributes to the eddy equilibration process (Qiu et al., 2008). Our fragmentary comprehension of the characteristics of the inverse KE cascade motivates this study.

Typical theories give different interpretations of the generation and evolution of eddies. The QG turbulence theory suggests that baroclinic instability is driven by mean quasigeostrophic potential vorticity (QGPV) gradient sign reversal and occurs in the deep ocean (~1 km) (Charney, 1971; Wang et al., 2019). It predicts a k^{-5} ($k^{-11/3}$) power law for sea surface height (SSH) wavenumber spectra in the inverse KE cascade (forward enstrophy cascade) regime (Kraichnan, 1967; Leith, 1968; Batchel-

---

Foundation item: The National Key R&D Program of China under contract Nos 2016YFC0301203 and 2019YFC1407903; the Natural Science Foundation of Hebei Province under contract No. D2019407046; the Hebei Science and Technology Project under contract No. 19273301D; the NSFC-Shangdong Province Joint Fund under contract No. U1406401.

*Corresponding author, E-mail: zhlliu3897@hevttc.edu.cn

or, 1969). Nevertheless, the surface quasigeostrophic (SQG) theory demonstrates that baroclinic instability is driven by an interaction of the mean surface gradient with a constant interior potential vorticity (PV) and dominated by surface intensified modes (about 100 m to 200 m) (Blumen, 1978). This theory correspondingly predicts SSH spectra following a $k^{-11/3}$ (k^{-3}) power law (Held et al., 1995). Hence, calculating the SSH spectral slope and comparing the results with theoretical predictions could clarify the applicability of the QG and SQG theories in real oceans, leading to further understanding of the characteristics and dynamics of the inverse KE cascade.

Related studies have intensively emerged with the development of satellite observations (Fu, 1983; Scott and Wang, 2005; Wortham IV, 2013; Le Traon et al., 2008; Vergara et al., 2019; Wang et al., 2019). The results suggest that the mesoscale wavenumber spectra of SSH are somewhat diverse, with spectral slopes ranging from approximately –11/3 to –5, depending on the local energy level (Fu, 1983; Le Traon et al., 2008; Xu and Fu, 2011, 2012; Khatri et al., 2018). However, no uniform conclusions regarding the efficacies of the QG and SQG theories have been presented until now. Thus, the characteristics of the KE inverse cascade are still unclear. Furthermore, most efforts have used a fixed wavelength band (i.e., 100–250 km for Fu (1983); 100–300 km for Le Traon et al. (2008); or 70–250 km for Xu and Fu (2011, 2012)). Actually, the length bands corresponding to the two inertial ranges vary globally (Eden, 2007; Wang et al., 2015), and the SSHs observed by altimeters are in an enstrophy cascade regime from approximately 200 km to 100 km and in an inverse KE transfer regime for scales greater than approximately 200 km in the mid-latitude oceans (Khatri et al., 2018). Thus, most of the related studies using altimeter data have not considered the difference between the two inertial ranges; consequently, the interpretations of the SSH spectral slopes may not be correct.

To further understand the dynamics of the mesoscale motions associated with the inverse KE cascade in the real oceans, we use high-resolution globally gridded sea level anomaly (SLA) data to revisit the wavenumber spectral characteristics over the scales of the inverse KE cascade. To identify the scale band associated with inverse KE cascade more accurately, an improved geographically dependent wavenumber band is defined to compute the global pattern of the SSH wavenumber spectral slope for the inverse KE cascade. The applicability of the QG and SQG theories in real oceans and the correlation between the slope value and eddy-kinetic-energy (EKE) are further discussed. Some new anisotropy characteristics of the mesoscale variabilities are also provided by comparing the statistical characteristics between the zonal and meridional wavenumber spectra.

This paper is organized as follows. The data and methods are described in Section 2. The geographic variability in the SSH wavenumber spectral slope and the relationship between the slope and EKE are shown in Section 3. In Section 4, we compare the zonal and meridional SSH wavenumber spectral slopes to analyze the anisotropic characteristics of the inverse cascade. In Section 5, comparisons are made with previous studies, followed by a discussion. The conclusions are given in the last section.

2 Data and methods

2.1 *Description of the dataset*

We used 20 years of the delayed gridded SLA product operated by the Data Unification and Altimeter Combination System (DUACS) and distributed by the Copernicus Marine Environment Monitoring Service (CMEMS). This dataset merges SSH measurements from 10 altimeter missions and deduces the long-term mean to yield the SLA data used in this research. Two versions of the dataset were used in this study. The version with a lower spatial ((1/3)° Mercator grid) and temporal resolution (7 d) but a lower error level was used to calculate the spectral KE flux, and the version with a higher spatial ((1/4)° Cartesian grid) and temporal resolution (1 d) but a higher error level (DT 2014) was used to calculate the SSH wavenumber spectra. The period of the two datasets ranges from 1993 to 2012.

The two datasets enable much better detection of mesoscale singles compared to using a single satellite (Pascual et al., 2006). One caveat is that the smoothing and interpolation techniques implemented during the gridding process cause energy attenuation at small scales, thereby limiting the capture capability of the gridded product (Le Traon et al., 1998). Thus, the spectra estimated using gridded data are steeper than those estimated using raw along-track data (Wortham IV, 2013; Wang et al., 2019). Fortunately, compared with the previous versions, the improvements in DT2014 reprocessing have led to a better effective resolution, reaching approximately 100 km at middle latitudes (Pujol et al., 2016). Furthermore, the noise in the measurements will shallow the spectra calculated using the raw along-track data (Xu and Fu, 2012). Indeed, the gridded data lead to SSH spectra with a similar shape to that obtained from along-track altimetry data, removing high-frequency noise (Zhou et al., 2015).

2.2 *Preprocessing the SLA data*

The data processing procedures are described as follows. First, 100-d high-pass filtering was used for the raw SLA to eliminate the wave signals (the reason for this operation is referenced in Appendix A). For the filtered SLA, a 10-d average was calculated first to remove high-frequency information that was not of interest. To avoid the influence of ice on the SSH measurements, the areas close to the polar sea (poleward of 60°S and 60°N) were excluded (Xu and Fu, 2011). Then, for each coordinate, a 10° × 10° box centered at the object point was selected for subsequent calculations (Qiu et al., 2008; Tulloch et al., 2011). The SLA field was detrended by fitting a linear plane by least squares and then subtracting the plane from the corresponding snapshot. To avoid slid-lobe power leakage, a Hanning window function was applied to all the detrended data in the box, such that each box tapered to zero at each edge. Points with more than 10% missing values in the corresponding box were omitted. Then, each box was cut into smaller boxes (9° × 9°), and each missing value was replaced by the average of the values of the 9 × 9 grid points centered on its position.

2.3 *SSH wavenumber spectrum and EKE*

2.3.1 *Scalar SSH wavenumber spectrum and EKE*

The 2-D SSH wavenumber spectra, $E_2(k_x,\ k_y)$, at each grid point were computed by fast Fourier transformation (FFT) for SLA, where k_x and k_y are the two orthogonal wavenumber components. The scalar SSH wavenumber spectra, $E_0(K)$, were calculated using the following function:

$$\int_0^{\infty} E_0(K)\mathrm{d}K = \int_{-\infty}^{+\infty}\int_{-\infty}^{+\infty} E_2(k_x, k_y)\mathrm{d}k_x\mathrm{d}k_y. \tag{1}$$

The discrete format is described as follows:

$$E_0(K) = \sum_{K=\sqrt{{k_x}^2+{k_y}^2}} E_2(k_x,\ k_y), \tag{2}$$

where K is the scalar wavenumber, defined as $K = ({k_x}^2 + {k_y}^2)^{1/2}$. Then, the time-averaged spectra, $E(K)$, at each grid point were computed.

Under the geostrophic balance, it was easy to calculate the geostrophic KE spectrum, $F(K)$, using the following relation (Fu, 1983):

$$F(K) = \frac{g^2}{2f^2}(2\pi K)^2 E(K), \tag{3}$$

where g is the gravity constant, $f = 2\Omega \sin\theta$ is the Coriolis parameter, Ω is the angular velocity of Earth's rotation, and θ is the geographical latitude. Integrating $F(K)$ over K yields the total EKE in the box:

$$\mathrm{EKE} = \int F(K)\mathrm{d}K = \int \frac{g^2}{2f^2}(2\pi K)^2 E(K)\ \mathrm{d}K. \tag{4}$$

2.3.2 *One-dimensional SSH wavenumber spectrum and EKE*

The meridional (zonal) SSH wavenumber spectrum for each grid was obtained by summing all the 2-D spectra in the box with wavenumber $k_y < k_x$ ($k_x < k_y$):

$$E_{\mathrm{m}}(K) = \sum_{k_y<k_x} E_2(k_x, k_y)\mathrm{d}k_x\mathrm{d}k_y, \tag{5}$$

$$E_{\mathrm{z}}(K) = \sum_{k_x<k_y} E_2(k_x, k_y)\mathrm{d}k_x\mathrm{d}k_y. \tag{6}$$

The meridional and zonal KE wavenumber spectra and EKE ($\mathrm{EKE_m}$ and $\mathrm{EKE_z}$) were computed using Eq. (4):

$$\mathrm{EKE_m} = \int \frac{g^2}{2f^2}(2\pi K)^2 E_{\mathrm{m}}(K)\ \mathrm{d}K, \tag{7}$$

$$\mathrm{EKE_z} = \int \frac{g^2}{2f^2}(2\pi K)^2 E_{\mathrm{z}}(K)\ \mathrm{d}K. \tag{8}$$

2.4 *Scalar spectral KE flux*

The geostrophic velocity anomalies can be estimated from the SLA data by assuming geostrophy:

$$u' = -\frac{g}{f}\frac{\partial \mathrm{SLA}}{\partial y}, \tag{9}$$

$$v' = \frac{g}{f}\frac{\partial \mathrm{SLA}}{\partial x}. \tag{10}$$

Following Wang et al. (2015), the spectral energy transfer can be calculated (detailed derivation is referred to Wang et al. (2015)):

$$\begin{aligned} T(k_x, k_y, t) =& \Re\left[\mathrm{fft}(u')^*\mathrm{fft}\left(u'\frac{\partial u'}{\partial x} + v'\frac{\partial u'}{\partial y}\right) + \right. \\ & \left. \mathrm{fft}(v')^*\mathrm{fft}\left(u'\frac{\partial u'}{\partial x} + v'\frac{\partial u'}{\partial y}\right)\right] \Big/ \Delta k^2, \end{aligned} \tag{11}$$

where $T(k_x, k_y, t)$ represents the transmission of EKE between the different spatial modes. The star indicates a complex conjugate. $\Delta k = 1/N\Delta x$ cpkm (cycles per kilometer), Δx is the grid spacing, and N is the number of grid points in each direction, as derived from the FFT. The KE flux at wavenumber K' can be computed by summing all the spectral energy transfer at modes (k_x, k_y) with $k_x^2 + k_y^2 > K'^2$:

$$\pi(K', t) = \sum_{K'^2<k_x^2+k_y^2} T(k_x, k_y, t)\Delta k^2. \tag{12}$$

The ratio of the magnitude of the inverse cascade KE to that of the total cascade KE (forward plus inverse cascade KE) can be further calculated using the time-averaged $\pi(K', t)$ (denoted as $\prod(K)$):

$$R = \text{ratio of inverse KE cascade} = \frac{\sum\limits_{\prod(K)<0} \left|\prod(K)\right| \Delta K}{\sum \left|\prod(K)\right| \Delta K}. \tag{13}$$

Figure 1a shows $\prod(K)$ calculated over the Kuroshio, the Gulf Stream, and the Agulhas regions. Consistent with the results of previous research, all $\prod(K)$ results have a prominent negative lobe that indicate an inverse KE cascade to smaller wavenumbers (Scott and Wang, 2005; Tulloch et al., 2011; Wang et al., 2015). Moreover, the wavelength at which the spectral flux crosses zero with a positive slope can be thought of as the energy injection scale L_{inj}, namely, the start of the inverse KE cascade. We also define the zero point at a large wavelength with a negative slope as the equilibration scale, L_{equ}, where the inverse KE cascade ends and eddies equilibrate. The percentage of the magnitude of the inverse cascade KE relative to that of the total cascade KE, R, is shown in Fig. 1b. Obviously, the inverse KE cascade is a robust feature of most oceans. It dominates the interscale energy transfer at high latitudes and the western boundaries, while it presents complex variation at low latitudes. It should be mentioned that limited by the resolution of the data, the domination of zero points in the spectral KE flux would produce large calculation errors. Thus, the spectral KE flux can only be used for qualitative analysis, and the L_{inj} and L_{equ} obtained from it is not accurate enough for the SSH spectral slope calculation.

2.5 *Variable wavelength range technique*

The inverse cascade band should be rationally determined before calculating the SSH wavenumber spectral slopes. The length scale of mesoscale eddies varies geographically, especially in the meridional direction (Jacobs et al., 2001). Thus, using a variable wavelength range to calculate the spectral slope is more reliable.

2.5.1 *Lower limit of the inverse cascade scales*

Generally, the deformation scale L_{r} is considered to be the energy injection wavelength, namely, the start of the inverse cascade (Scott and Wang, 2005). Unfortunately, it is smaller than the effective resolution of DT2014 SLA at mid-high latitudes; hence, we can only use the real L_{r} value in equatorial areas. Using SSH fields observed by altimeters, Chelton et al. (2011) computed a speed-based eddy scale L_{s}. This observed scale is larger than L_{r} in the extratropics, nearly achieving an effective resolution in most oceans (Fig. 12 in Chelton et al., 2011). Moreover, Chelton et al. (2011) did not show precise L_{s} values in equatorial regions (5°S–5°N). In this context, L_{r} is replaced by L_{s} in the extratropics to en-

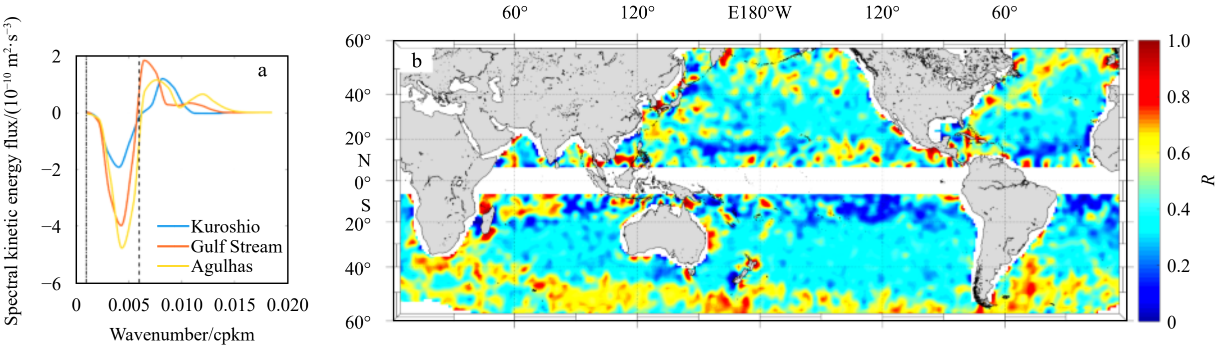

Fig. 1. Time-averaged scalar spectral KE flux versus the wavenumber in the Kuroshio (centered at 35°N, 144°E), the Gulf Stream (centered at 39°N, 64°W), and the Agulhas (centered at 40°S, 19°E) regions (a); and the percentage of the magnitude of the inverse cascade KE relative to that of the total cascade KE (R, b). In a, the vertical dashed line is $L_{\rm inj}$, and the vertical dash-dotted line is $L_{\rm equ}$. cpkm: cycles per km.

sure that the calculation band of the spectrum is not distorted. The shortening of the calculation band does not affect the results significantly because the slope of the inverse cascade is almost constant.

In short, the lower limit of the inverse cascade used in this paper, $L_{\rm low}$(the corresponding wavenumber is recorded as $K_{\rm low}$), is a combination of $L_{\rm s}$ calculated by Chelton et al. (2011) and $L_{\rm r}$ calculated by Chelton et al. (1998):

$$L_{\rm low} = \begin{cases} L_{\rm r}, & \text{for } 5^\circ\text{S}-5^\circ\text{N}; \\ L_{\rm s}, & \text{for the other regions.} \end{cases} \tag{14}$$

2.5.2 *Upper limit of the inverse cascade scales*

At scales larger than the halting scale L_0, the energy dissipated by the frictional effect is balanced by the energy transferred through the inverse cascade, such that the KE spectrum and the corresponding SSH spectrum peak at L_0 (Vallis, 2007). In this paper, the wavelength corresponding to the spectral peak is used as the upper limit of the inverse cascade.

The global distribution of the magnitude of EKE (m²/s²), lg(EKE), is shown in Fig. 2. Notably, Eq. (3) is invalid in the equatorial area (5°S–5°N) because the motions there are ageostrophic (Tchilibou et al., 2018). Thus, the EKE value is not shown, but the SSH spectrum is credible here. Furthermore, baroclinic instability is inhibited in equatorial areas, while barotropic instability is more important (Qiu and Chen, 2004), and the motion is dominated by a wavelike regime (Fu, 2004; Theiss, 2004; Chelton et al., 2007).

As revealed in Fig. 2, the EKE around predominantly eastward flowing currents, such as the Kuroshio Extension, the Gulf Stream, the Subtropical Countercurrent (STCC), and the Antarctic Circumpolar Current (ACC), is generally 1 to 2 orders of magnitude higher than that in the eastern basin. The Northeast Pacific and the Southeast Pacific are two distinct low-value areas. The eastern subtropical Pacific, especially in the Northern Hemisphere, has a higher EKE level compared to the surrounding area. Based on this trait, several typical positions were selected for the analysis of the shape of the wavenumber spectrum: the local

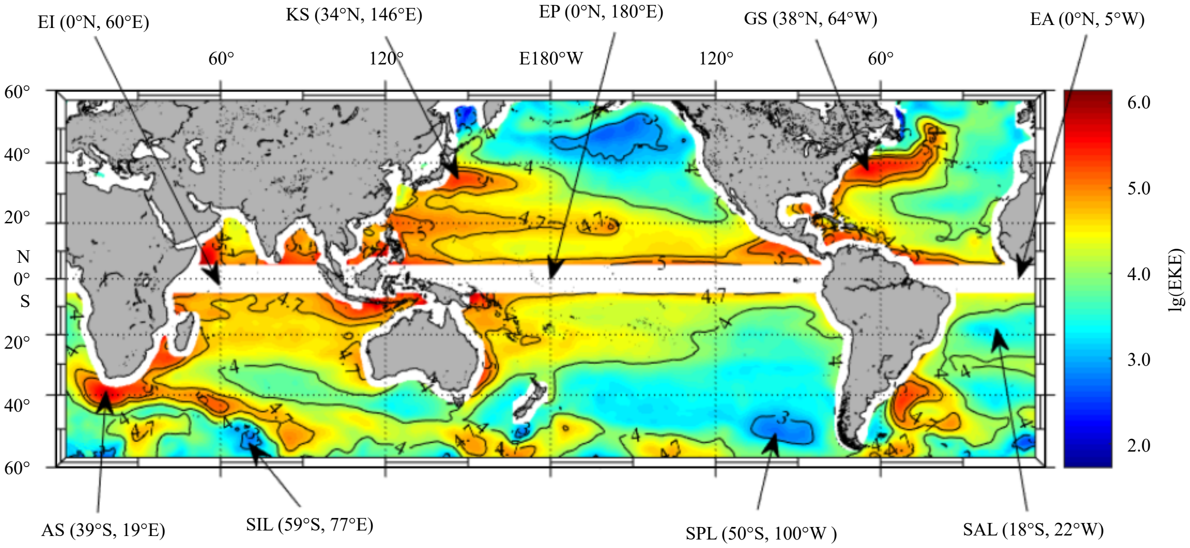

Fig. 2. The global distribution of lg(EKE). The points marked with arrows are the typical positions selected for subsequent analyses. EI: the equatorial point in the Indian Ocean, KS: Kuroshio, EP: the equatorial point in the Pacific Ocean, GS: Gulf Stream, EA: the equatorial point in the Atlantic Ocean, AS: Agulhas Current, SIL: the low-EKE point in the South Indian Ocean, SPL: the low-EKE point in the South Pacific Ocean, SAL: the low-EKE point in the South Atlantic Ocean.

maximum points of the Kuroshio (KS), the Gulf Stream (GS) and the Agulhas Current (AS), which represent high-EKE regions; three equatorial points in the Indian Ocean (EI), the Pacific Ocean (EP) and the Atlantic Ocean (EA), which represent regions in which it is difficult to distinguish the signals of waves and eddies; and three common low-EKE points in the South Indian Ocean (SIL), South Pacific Ocean (SPL) and South Atlantic Ocean (SAL).

Figure 3 shows the SSH wavenumber spectra in the typical positions selected above. In the high (Fig. 3a)- and low (Fig. 3c)-EKE level regions, the spectra are characterized by a broad peak at wavelengths from 250 km to 350 km and a maximum at approximately 300 km, showing a "red" spectrum at shorter wavelengths and a slight "blue" spectrum at longer wavelengths①. In equatorial regions (Fig. 3b), the spectrum is "red" at all wavelengths without a peak. It is worth mentioning that positions with higher EKE levels show larger amplitudes in their SSH spectra, which can be understood based on Eq. (4). This positive relationship is obvious in the comparison between Figs 3a, b and c.

In conclusion, the maximum spectrum occurs at approximately 300 km, except in the equatorial region, which has a "red" spectrum at all wavelengths. In this case, we used the wavelength corresponding to the highest power density in the SSH wavenumber spectrum as the upper limit, L_{up} (the corresponding wavenumber is recorded as K_{up}), in equatorial areas (10°S–10°N) and a constant, 300 km, in other areas.

Based on the discussions above, the definition of a variable wavelength range is shown in Fig. 4. The observed and theoretical inverse KE cascade bands are also shown to confirm that they cover the band used in the following slope calculations. The observed start scale of the inverse KE cascade (L_{inj}) is slightly larger than its theoretical value (the Rossby deformation scale L_{r}). The lower limit of the wavelength band used to calculate the spectral slope in this study is sandwiched between the observed and theoretical values and is closer to L_{inj}, while the upper limit is lower than the end scale of the inverse KE cascade. Thus, it could be considered that the wavelength band used to calculate the spectral slope belongs to the inverse KE cascade band.

3 Characteristics of the SSH wavenumber spectral slope for the inverse KE cascade

3.1 *Global variability for the SSH wavenumber spectral slope*

The slope of the SSH wavenumber spectrum calculated in Section 2 is an intuitive manifestation of the generation of mesoscale eddies and the strength of the inverse KE cascade. A higher absolute value of the slope (referred to as a "steeper slope" in the following text), namely, a steeper spectrum, implies that eddies will transfer more KE upscale per unit wavelength band, which is described as a faster (or stronger) inverse KE cascade in the fol-

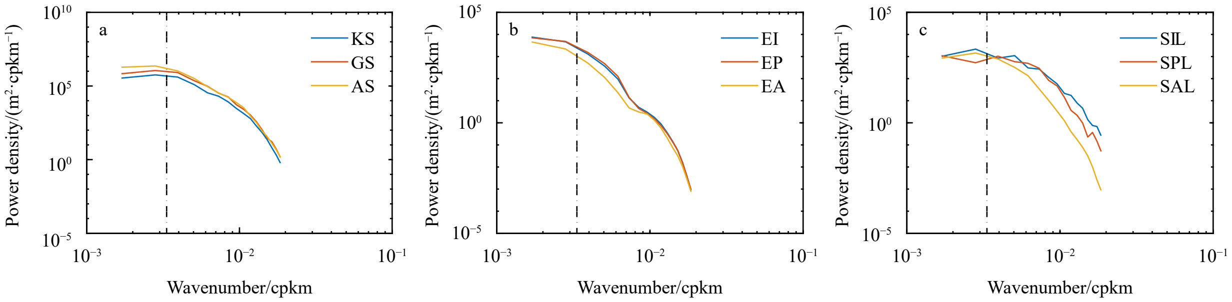

Fig. 3. Time-averaged scalar SSH wavenumber spectrum in high-EKE regions (a), equatorial regions (b), and other low-EKE regions (c). The black dotted line indicates wavelengths of 300 km. KS: Kuroshio, GS: Gulf Stream, AS: Agulhas Current, EI: the equatorial point in the Indian Ocean, EP: the equatorial point in the Pacific Ocean, EA: the equatorial point in the Atlantic Ocean, SIL: the low-EKE point in the South Indian Ocean, SPL: the low-EKE point in the South Pacific Ocean, SAL: the low-EKE point in the South Atlantic Ocean. cpkm: cycles per km.

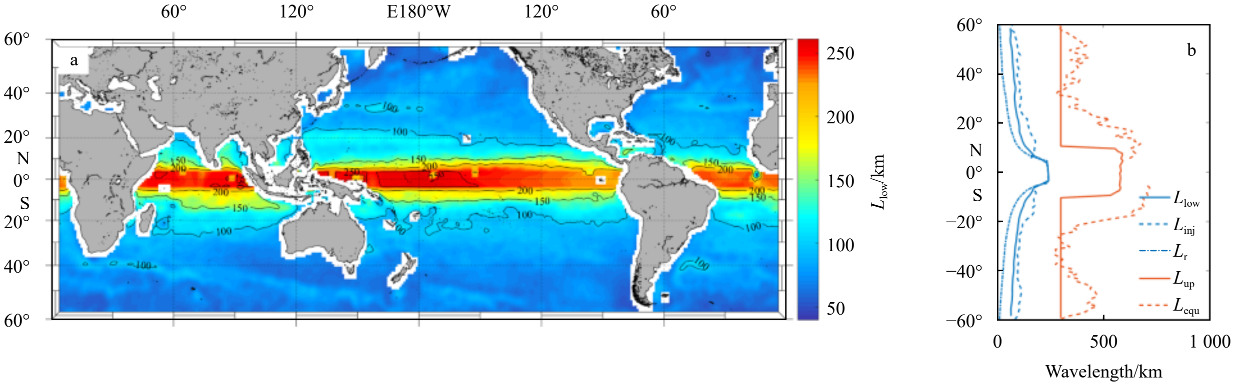

Fig. 4. Spatial distribution of the lower limit (L_{low}, a) and the zonal average of the lower (blue solid) and upper (orange solid) limits of the variable wavelength range used to fit the spectral slope (b). The Rossby deformation scale L_{r} (blue dash-dot), the energy injection scale L_{inj} (blue dash), and the eddy equilibration scale L_{equ} (orange dash) used to detect the inverse KE cascade band are shown.

---

①A "red (blue)" spectrum is defined as a spectrum in which the power density decreases (increases) with the wavenumber.

lowing discussion. Figure 5a demonstrates the global distribution of the SSH wavenumber spectral slope for the inverse KE cascade. For the vast mid-latitude oceans, which have been suggested to be geostrophically turbulent oceans (Stammer, 1997), the slopes have a wide range of –1.00 to –5.50. The predominantly eastward flowing currents (such as the Kuroshio Extension and the GS, STCC and ACC), the AS Current, the South Indian Ocean and the Brazilian Current, in which the dynamics are highly nonlinear (Chelton et al., 2011), may exhibit a much stronger inverse KE cascade than other areas. Specifically, the spectral slopes are steeper than –5 in the core of the high-EKE regions and flatter than –3.50 in the low-EKE regions of the tropics, the eastern basin of the Pacific Ocean and areas of the Atlantic Ocean away from the mean currents.

Notably, unlike in previous works, we shifted our focus to those characteristics associated with the inverse KE cascade, for which the slope value predicted by the QG and SQG theory are –11/3 and –3, respectively. Figure 5b shows the areas where the spectral slopes follow the QG $k^{-11/3}$ (red) and the SQG k^{-3} (blue) power law within the 95% confidence level. Thus, based on our research, the results for the inverse cascade process could be obtained. At mid-high latitudes with high-EKE, the isopycnals slope upward to the pole, and the QGPV gradient (Q_y) changes its sign in the deep ocean (Tulloch et al., 2011). The QG turbulence theory is a better dynamic framework. Thus, the inverse KE cascade tends to present a $k^{-11/3}$ power law in the SSH spectrum at the edges of these regions. In tropical regions, the isopycnals slope upward to the equator, and the β-effect is significant, baroclinic instability is driven by the interaction of the mean surface temperature gradient with β (Tulloch et al., 2011). Thus the SQG theory is a suitable dynamic, and the inverse KE cascade tends to present a k^{-3} power law in the SSH spectrum in these areas. However, the QG and SQG theories are highly simplified frames, which do not consider the complex processes in the real oceans such as stratification, the formation of coherent structures, the bottom topography, etc. (Charney, 1971; Blumen, 1978; Scott and Wang, 2005). Moreover, typical oceanic velocity profiles contain a mix of both surface and nonconstant interior gradients. Thus, the QG and SQG theory do not always apply.

Overall, the SSH wavenumber spectral slope for the inverse KE cascade band is positively correlated with the local EKE level. However, there are two particular regions in the Northeast and Southeast Pacific, respectively, which have low EKE levels but steep slopes (framed with blue boxes in Fig. 5a). The two regions fit well with the “eddy desert” reported by Chelton et al. (2007), whose central position lies at (50°N, 160°W) and (50°S, 95°W), respectively. They are regions lacking mesoscale eddies and dom-

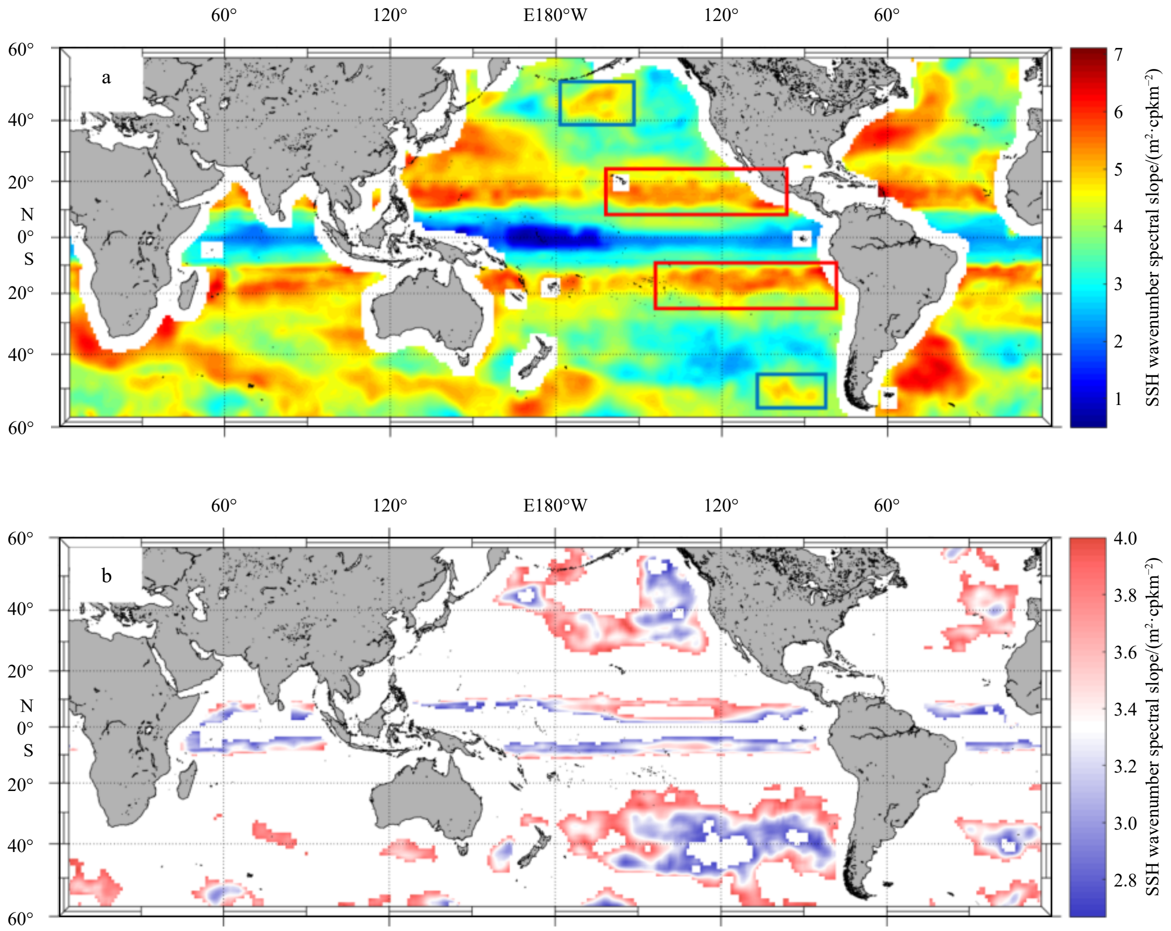

Fig. 5. The global distribution of the SSH wavenumber spectral slopes for the inverse KE cascade inertial range. In a, the blue (red) boxes frame the “eddy desert” (subtropical Pacific) regions analyzed in Fig. 6b (Fig. 8); in b, there are three types of areas in terms of the spectral power law. The red color represents regions with spectral slopes following the QG $k^{11/3}$ power law within the 95% confidence level, and the blue color represents regions with spectral slopes following the SQG k^{-3} power law. For comparison with the map made by predecessors, the signs of the slopes were reversed to ensure that most values were positive. cpkm: cycles per km.

inated by a wave regime (Stammer, 1997; Liu and Pang, 2017). The inverse KE cascade in these regions is consistent with the QG theory at the edge (Fig. 5b).

3.2 *Relationship between SSH spectral slope and EKE*

Figures 2 and 5a show an obvious relationship between the value of the SSH spectral slope and the local EKE. To further explore their relationship, the SSH wavenumber spectra at high (solid)- and low (dotted)-EKE level positions were compared in Fig. 6a. The spectra in "eddy desert" regions are also shown to explain the particular phenomenon that occurs (Fig. 6b). It should be mentioned that the values of the EKE and slope are shown in the figures for clear analysis. In most oceans, the power densities at the lower limit scales ($E(K_{\rm low})$) are similar in different EKE-level regions, and the power density at the upper limit scales ($E(K_{\rm up})$) is higher in high-EKE regions. In "eddy desert" regions, the energy injection scales contain lower power densities compared to the adjacent regions with higher EKE levels, and the equilibration scales contain similar power densities in different EKE-level regions.

The SSH spectral slope is recorded as $-S(K)$, and

$$S(K) = -\frac{{\rm d}(\lg E(K))}{{\rm d}(\lg K)}. \tag{15}$$

For the inverse KE cascade band ($K_{\rm up} < K < K_{\rm low}$),

$$-S(K) = -S_0 = \frac{\lg E(K_{\rm low}) - \lg E(K_{\rm up})}{\lg K_{\rm low} - \lg K_{\rm up}} < 0, \tag{16}$$

where S_0 is the slope of the inverse KE cascade that we calculated in Section 3, which is a constant for different wavenumbers at a specified location.

3.2.1 *For most of the oceans*

As mentioned above, $E(K_{\rm low})$ values are very similar in different EKE-level regions. Thus, for $K \in [K_{\rm up}, K_{\rm low}]$:

$$\begin{cases} \lg E(K) = \lg E(K_{\rm low}) + S_0(\lg K_{\rm low} - \lg K), \\ E(K) = E(K_{\rm low})\left(\dfrac{K_{\rm low}}{K}\right)^{S_0}. \end{cases} \tag{17}$$

Then,

$$E(K_{\rm up}) = E(K_{\rm low})\left(\frac{K_{\rm low}}{K_{\rm up}}\right)^{S_0}. \tag{18}$$

By substituting Eqs (17) and (18) into Eq. (4), and taking the integral from the minimum wavenumber observed in the box, $K_{\rm min}$, to the maximum one, $K_{\rm max}$, the following is obtained:

$$\begin{aligned} {\rm EKE} = & \int_{K_{\rm min}}^{K_{\rm max}} \frac{{\rm g}^2}{2f^2}(2\pi K)^2 E(K){\rm d}K \\ =& 2\left(\frac{\pi {\rm g}}{f}\right)^2 \left\{ \int_{K_{\rm min}}^{K_{\rm up}} K^2 E(K){\rm d}K + \int_{K_{\rm up}}^{K_{\rm low}} K^2 E(K_{\rm low}) \times \right. \\ & \left. \left(\frac{K_{\rm low}}{K}\right)^{S_0} {\rm d}K + \int_{K_{\rm low}}^{K_{\rm max}} K^2 E(K){\rm d}K \right\} \\ =& 2\left(\frac{\pi {\rm g}}{f}\right)^2 \left\{ \int_{K_{\rm min}}^{K_{\rm up}} K^2 E(K){\rm d}K + {K_{\rm low}}^{-2} E(K_{\rm low}) \times \right. \\ & \left. \int_{K_{\rm up}}^{K_{\rm low}} \left(\frac{K_{\rm low}}{K}\right)^{S_0+2} {\rm d}K + \int_{K_{\rm low}}^{K_{\rm max}} K^2 E(K){\rm d}K \right\}. \end{aligned} \tag{19}$$

From the SSH spectrum (Fig. 3, Fig. 6), it can be regarded that $E(K) \approx E(K_{\rm up})$ for $K < K_{\rm up}$, and $\int_{K_{\rm low}}^{K_{\rm max}} K^2 E(K){\rm d}K$ is a small term compared with other two and is ignored here. Therefore,

$$\begin{aligned} \lg {\rm EKE} \approx & \lg \left\{ 2\left(\frac{\pi {\rm g}}{f}\right)^2 \left[\int_{K_{\rm min}}^{K_{\rm up}} K^2 E(K_{\rm up}){\rm d}K + \right.\right. \\ & \left.\left. {K_{\rm low}}^{-2} E(K_{\rm low}) \int_{K_{\rm up}}^{K_{\rm low}} \left(\frac{K_{\rm low}}{K}\right)^{S_0+2} {\rm d}K \right] \right\} \\ = & \lg \left\{ 2\left(\frac{\pi {\rm g}}{f}\right)^2 \left[\frac{1}{3}({K_{\rm up}}^3 - {K_{\rm min}}^3) E(K_{\rm low}) \left(\frac{K_{\rm low}}{K_{\rm up}}\right)^{S_0} + \right.\right. \\ & \left.\left. {K_{\rm low}}^{-2} E(K_{\rm low}) \int_{K_{\rm up}}^{K_{\rm low}} \left(\frac{K_{\rm low}}{K}\right)^{S_0+2} {\rm d}K \right] \right\}. \end{aligned} \tag{20}$$

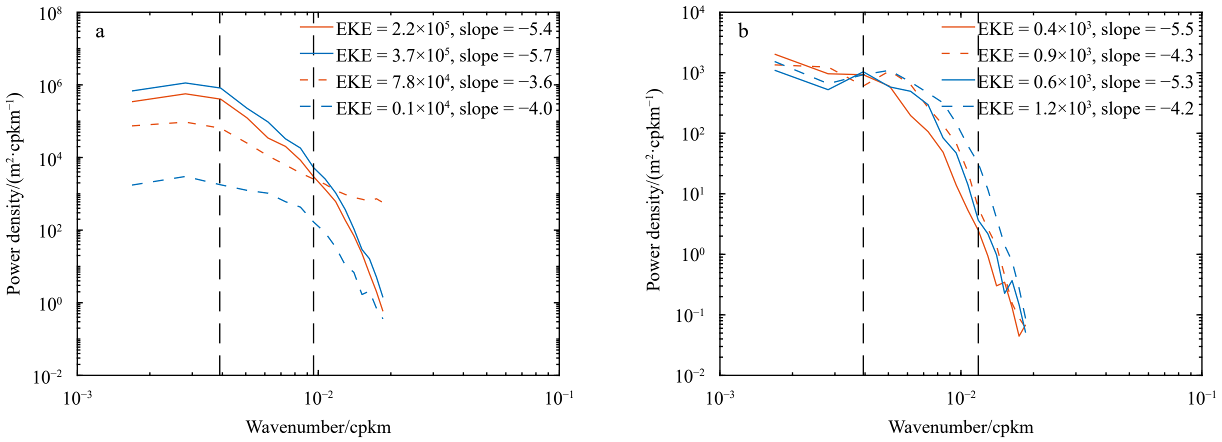

Fig. 6. Time-averaged scalar SSH wavenumber spectra at the Kuroshio centered at (35°N, 146°E) (red solid), the Gulf Stream centered at (39°N, 64°W) (blue solid), the region around the Kuroshio but with a low-EKE level centered at (31°N, 134°E) (red dotted) and the region around the Gulf Stream with a low-EKE level centered at (56°N, 47°W) (blue dotted) (a). Time-averaged scalar SSH wavenumber spectra with the regionally steepest slope (–5.5 and –5.3 respectively) at the "eddy deserts" (marked with blue boxes in Fig. 5a) (solid) and the adjacent regions (dotted). The four regions centered at (48°N, 162°W) (red solid), (42°N, 159°W) (red dotted), (51°S, 101°W) (blue solid), and (46°S, 96°W) (blue solid) (b). The black dotted line indicates the upper and lower limit wavelengths, respectively. cpkm: cycles per km.

Let

$$A=\frac{2}{3}\left(\frac{\pi g}{f}\right)^2({K_{\rm up}}^3-{K_{\rm min}}^3)E(K_{\rm low})>0, \tag{21}$$

$$B=2\left(\frac{\pi g}{f}\right)^2{K_{\rm low}}^{-2}E(K_{\rm low})>0, \tag{22}$$

$$\alpha=A\left(\frac{K_{\rm low}}{K_{\rm up}}\right)^{S_0}, \tag{23}$$

$$\beta=B\int_{K_{\rm up}}^{K_{\rm low}}\left(\frac{K_{\rm low}}{K}\right)^{S_0+2}{\rm d}K, \tag{24}$$

thus,

$$\begin{aligned}\lg {\rm EKE}\approx&\lg\left\{2\left(\frac{\pi g}{f}\right)^2\left[\int_{K_{\rm min}}^{K_{\rm up}}K^2E(K_{\rm up}){\rm d}K+\right.\right.\\&\left.\left.{K_{\rm low}}^{-2}E(K_{\rm low})\int_{K_{\rm up}}^{K_{\rm low}}\left(\frac{K_{\rm low}}{K}\right)^{S_0}{\rm d}K\right]\right\}\\=&\lg\left[A\left(\frac{K_{\rm low}}{K_{\rm up}}\right)^{S_0}+B\int_{K_{\rm up}}^{K_{\rm low}}\left(\frac{K_{\rm low}}{K}\right)^{S_0+2}{\rm d}K\right]\\=&\lg(\alpha+\beta).\end{aligned} \tag{25}$$

We have $\left(\frac{K_{\rm low}}{K_{\rm up}}\right)>1$ and $A>0$; thus, $\alpha\propto S_0$. For $K\in[K_{\rm up},K_{\rm low}]$, $\frac{K_{\rm low}}{K}>1$; thus, $\beta\propto S_0$.

In summary,

$$\lg {\rm EKE}\propto S_0, \tag{26}$$

namely, lg(EKE) is positively correlated with S_0.

3.2.2 *For the “eddy desert” regions*

In the “eddy desert” regions, $E(K_{\rm low})$ is different, while $E(K_{\rm up})$ shows similar values. Thus, for $K\in[K_{\rm up},K_{\rm low}]$,

$$\left\{\begin{aligned}&\lg E(K)=\lg E(K_{\rm up})-S_0(\lg K-\lg K_{\rm up}),\\&E(K)=E(K_{\rm up})\left(\frac{K_{\rm up}}{K}\right)^{S_0}.\end{aligned}\right. \tag{27}$$

By substituting Eqs (27) and (18) into Eq. (4) and taking integral of the wavenumber, the following is obtained:

$$\begin{aligned}\lg {\rm EKE}\approx&\lg\left\{2\left(\frac{\pi g}{f}\right)^2\left[E(K_{\rm up})\int_{K_{\rm min}}^{K_{\rm up}}K^2{\rm d}K+\right.\right.\\&\left.\left.\int_{K_{\rm up}}^{K_{\rm low}}K^2E(K_{\rm up})\left(\frac{K_{\rm up}}{K}\right)^{S_0}{\rm d}K\right]\right\}\\=&\lg\left\{2\left(\frac{\pi g}{f}\right)^2\left[\frac{1}{3}({K_{\rm up}}^3-{K_{\rm min}}^3)E(K_{\rm up})+\right.\right.\\&\left.\left.{K_{\rm up}}^{-2}E(K_{\rm up})\int_{K_{\rm up}}^{K_{\rm low}}\left(\frac{K_{\rm up}}{K}\right)^{S_0+2}{\rm d}K\right]\right\},\end{aligned} \tag{28}$$

$$\lg {\rm EKE}\propto\lg\left(\frac{K_{\rm up}}{K}\right)(S_0+2). \tag{29}$$

For $K\in[K_{\rm up},K_{\rm low}]$, $\frac{K_{\rm up}}{K}<1$; thus, $\lg\frac{K_{\rm up}}{K}<0$, and lg(EKE) is negatively correlated with S_0.

Dynamically, nearly all of the world ocean is baroclinically unstable (Spall, 2000; Arbic and Flierl, 2004; Smith, 2007), through which large-scale flows feed energy into mesoscale eddies. The eddies at the injection scales contain similar EKE levels, while steeper spectral slopes imply more intense inverse KE cascades, through which the nonlinear triad interaction causes greater KE transfer within the phase space. Thus, larger eddies obtain more KE from the inverse KE cascade, and the integral EKE in the regions with a steeper slope is larger. In contrast, linear dynamics (wave motions) are dominant in the “eddy desert” regions, in which the eddies are prevented from growing larger (Chelton et al., 2007, 2011; Liu and Pang, 2017). Thus, weaker inverse KE cascades and flatter slopes are expected in these areas, which is inconsistent with Fig. 6b. A possible explanation for this phenomenon comes from Fig. 6b and Eq. (29). The “eddy desert” regions are dominated by the wave regime. The relatively larger-scale motions there contain similar energy levels. Thus, the lower is the smaller-scale energy, the steeper is the spectral slope.

The scatter diagram between lg(EKE) and S_0 shows the linear correlation clearly (Fig. 7). Notably, the values in the equatorial area (10°S to 10°N), where the quasigeostrophic relationship is invalid, and the polar regions (with latitudes higher than 60°), where the ice influence on observations could not be ignored, were not considered. Figure 7 shows that the SSH spectral slope is strongly related to the lg(EKE), as Eqs (26) and (29) show. The correlation coefficient at the 95% confidence level (represented by “r” in the following discussion) is approximately 0.67, which indicates a significant correlation. The first fitting was performed for the scatters, with a root mean square error (RMSE) of 0.60.

The differently colored scatter points in Fig. 7a are obviously inconsistent with the fitted curve. The scatter diagrams of the “eddy desert” in the Northeast and Southeast Pacific are shown in Figs 7c and d, respectively, which suggest that the scatter points for those regions are contrary to the global trend. The scatter diagram in other low-EKE ($<10^{3.2}$ m^2/s^2) areas (Fig. 7e) indicates that the spectral slope shows no obvious dependence on the lg(EKE). Figure 7b shows a scatter diagram in the global ocean excluding the scatters shown in Figs 7c, d, and e, and r improves to 0.71, while the RMSE of the first fitting is reduced to 0.57.

In conclusion, the absolute magnitude of the slope and lg(EKE) show an obvious linear positive correlation in most of the oceans, except in the “eddy desert” regions, where they are negatively correlated, and in the areas with very low EKE levels ($<10^{3.2}$ m^2/s^2), where they have no significant correlation.

3.3 ***Spectral slope in the eastern subtropical Pacific***

The eastern subtropical Pacific deserves a special discussion because it has the locally steepest slope (framed with red boxes in Fig. 5a), which was significant in our result but not in previous works (Xu and Fu, 2011, 2012; Vergara et al., 2019). As presented in Fig. 2, the eastern subtropical Pacific, especially the portion in the Northern Hemisphere, has a higher EKE level compared to the surroundings. This area has been suggested to have strong baroclinic instability and energetic nonlinear motions (Chelton et al., 2011; Wang et al., 2015). Hence, the inverse cascade of eddies is energetic in the eastern subtropical Pacific, which implies steep slopes that are consistent with our results. For further exploration, the SSH wavenumber spectra in the eastern subtropical Pacific are compared with the SSH wavenumber spectra in the adjacent regions with common EKE levels in Fig. 8.

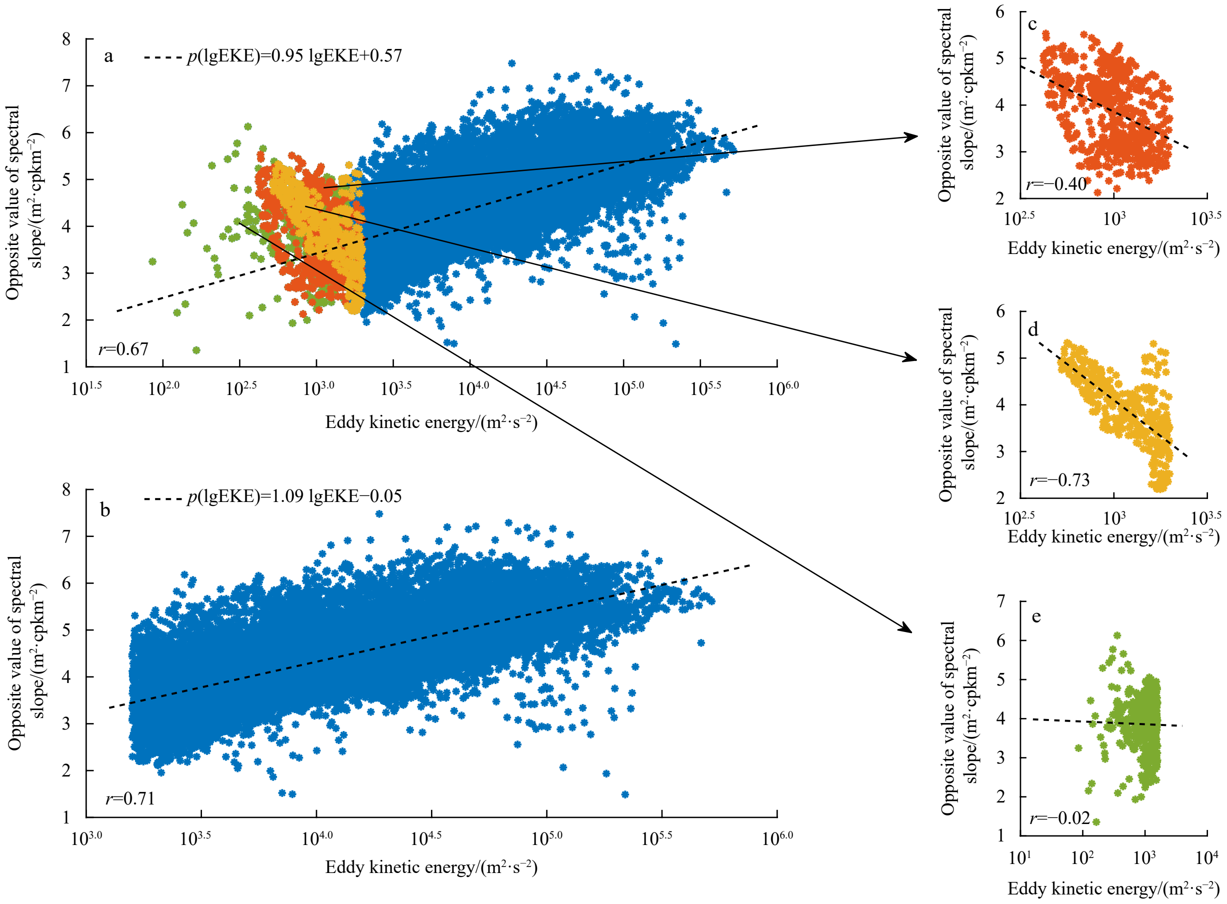

Fig. 7. Scatter diagram between the EKE order of magnitude and the inverse of the wavenumber spectral slope in the global ocean (a), the global ocean without the "eddy deserts" and areas with an EKE lower than $10^{3.2}$ m^2/s^2 (b), the "eddy desert" in the North Pacific (c), the "eddy desert" in the South Pacific (d), and other areas with an EKE lower than $10^{3.2}$ m^2/s^2 (e). The dotted line is the first-order fitting for the scatters. cpkm: cycles per km.

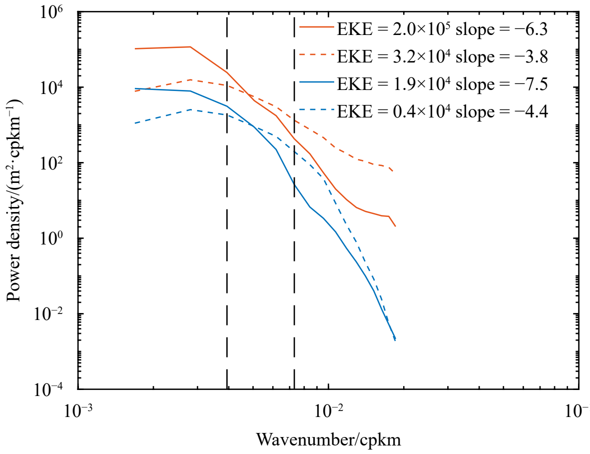

Fig. 8. Time-averaged scalar SSH wavenumber spectra with the steepest slope (-6.3 and -7.5 respectively) in the eastern subtropical Pacific (solid) (framed with red boxes in Fig. 5a) and adjacent regions (dotted). The four regions are centered at (11°N, 93°W) (red solid), (20°N, 109°W) (red dotted), (11°S, 84°E) (blue solid), and (20°S, 100°W) (blue dotted). The black dotted line indicates the upper and lower limit wavelengths. cpkm: cycles per km.

According to Eq. (16),

$$S_0 = \frac{\lg E(K_{\rm up}) - \lg E(K_{\rm low})}{\lg K_{\rm low} - \lg K_{\rm up}}. \tag{30}$$

The eastern subtropical Pacific has the same value of $\lg K_{\rm low} - \lg K_{\rm up}$(Fig. 8). The lower power densities at injection scales ($E(K_{\rm low})$) and the higher power densities at equilibration scales ($E(K_{\rm up})$) work together to cause a high value of $\lg E(K_{\rm up})-\lg E(K_{\rm low})$ and, thus, a steep slope. Based on Eq. (4), the higher $E(K_{\rm up})$ might be the main factor affecting the high EKE level here.

4 Anisotropy of the wavenumber spectrum

The inverse KE cascade becomes anisotropic when the change in the Coriolis parameter with latitude, namely, the β-effect, is introduced (Rhines, 1975, 1979; Theiss, 2004; Galperin et al., 2010; Wang et al., 2015). Hence, the along-track spectrum used by previous studies cannot fully reveal the dynamics of mesoscale variabilities, especially for scales large enough to feel the β-effect. This section will discuss the anisotropic characteristics of the entire SSH wavenumber spectrum and only the inverse cascade band. The meridional and zonal SSH wavenumber spectra were calculated as the method of Section 2.3.2. Figures 9a and b depict a comparison of the zonal and meridional spectral slopes (recorded as $S_{\rm z}$ and $S_{\rm m}$, respectively). Note that these one-

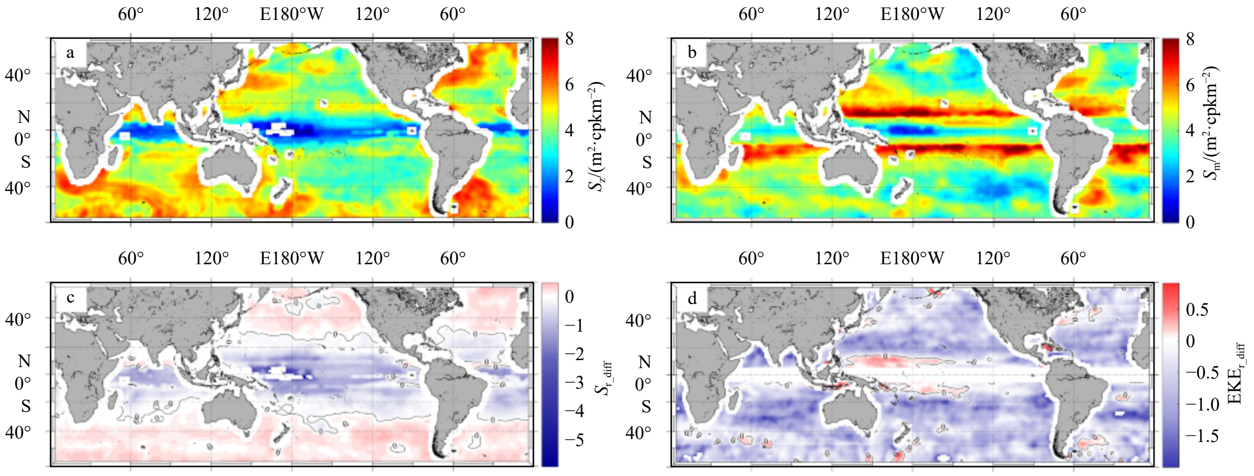

Fig. 9. Zonal (S_z, a), and meridional (S_m, b), SSH wavenumber spectral slopes calculated in the same variable wavelength band as the scalar spectrum, and maps of the relative differences between S_z and S_m (S_{r_diff}, c), as well as relative differences between EKE_z and EKE_m (EKE_{r_diff}, d).

dimensional spectral slopes were computed at the same variable wavelength band used for the scalar spectrum. Here, the relative differences, S_{r_diff} and EKE_{r_diff}, are shown simultaneously (Figs 9c and d), and they were computed as follows:

$$S_{r\_diff} = (S_z - S_m)/S_z, \tag{31}$$

$$EKE_{r\_diff} = (EKE_z - EKE_m)/EKE_z. \tag{32}$$

Clearly, anisotropy of the inverse cascade exists in the global ocean and is significant in the tropics, consistent with Stewart et al. (2015) (Fig. 9c). Specifically, S_z is slightly steeper than S_m at latitudes higher than 30° and significantly smoother at low latitudes, especially near 10° (Fig. 9c), implying that the zonal (meridional) inverse cascade of the baroclinic KE is stronger at high (low) latitudes. Furthermore, the geographical distributions of the zonal and meridional spectral slopes share a similar spatial pattern with the gridded spectral slopes, except in subtropical areas, where the meridional slope is significantly steeper. This effect might be due to the seasonal meridional oscillation of the equatorial current system (Peterson and Stramma, 1991; Bourles et al., 1999), which increases the large-scale meridional energy and leads to the overestimation of the meridional slope. Focusing on the entire spectra, $EKE_z > EKE_m$ at low latitudes (5° to 15°) and a few spots around the ACC and western boundary currents, whereas $EKE_z < EKE_m$ at mid-high latitudes away from zonal currents. Interestingly, the entire spectra tend to be isotropic in high-EKE regions.

To explore the reasons for the anisotropic characteristics, a comparison between zonal and meridional SSH spectra in typical regions is shown in Fig. 10. In the tropics, the meridional energy is lower than the zonal energy at eddy-dominant scales. This finding implies that eddies are stretched zonally and contribute to flattening the zonal spectrum (Figs 10d, e and f). Indeed, observations have demonstrated that mesoscale signals tend to become zonally elongated due to the β-effect (Wang et al., 2015). Around the strong zonal currents in the tropics and western boundaries, the meridional energy is higher than the zonal energy at large scales (Figs 10a–f). This phenomenon might be caused by the meridional oscillation of predominant zonal currents, which could also be observed as large-scale meridional energy in altimeter observations. These meridionally elongated large-scale signals also contribute to steepening of the meridional spectrum in the tropics. However, in the high-EKE areas around the western boundary currents, the meridional slope is not affected because the meridionally elongated scales exceed the slope calculation band. In terms of EKE, in the tropics, the higher zonal energy at eddy-dominant scales not only offsets the higher meridional energy at large scales but also ultimately results in a higher zonal integral EKE. Meanwhile, in the high-EKE areas around the western boundary currents, the zonal elongation of eddies is not so significant that the integral EKE is higher in the meridional direction. Determining the dynamics of the anisotropic characteristics is an interesting task and requires further research.

Moreover, the anisotropy of the inverse cascade might cause a loss of information from the one-dimensional spectra. Hence, the along-track spectrum used by previous studies cannot reveal the dynamics of the mesoscale variabilities well, and the scalar spectrum is more suitable for answering this question.

5 Comparison and discussion

5.1 *Wavelength band selection for slope calculation*

In recent years, the importance of globally variable mesoscale wavelength ranges for mesoscale eddy research has been gaining recognition. Vergara et al. (2019) used the minimum value between the local Rhines scale (L_R) and L_r as the lower wavelength limit in a related study. However, L_R is regarded to be the equilibrated scale between the nonlinear turbulence and linear Rossby waves, at which the inverse KE cascade is halted (Liu and Pang, 2017; Vallis and Maltrud, 1993). Considering L_R as the lower limit of the slope calculation band at which the inverse KE cascade initially starts might be physically unreasonable. Wang et al. (2019) used an artificially lower limit defined as a function of the upper limit, which is somewhat subjective. More realistically and objectively, the slope calculation wavelength band used in this paper has an upper limit that is similar to those in previous studies and a lower limit that is replaced by the eddy scale observed by Chelton et al. (2011).

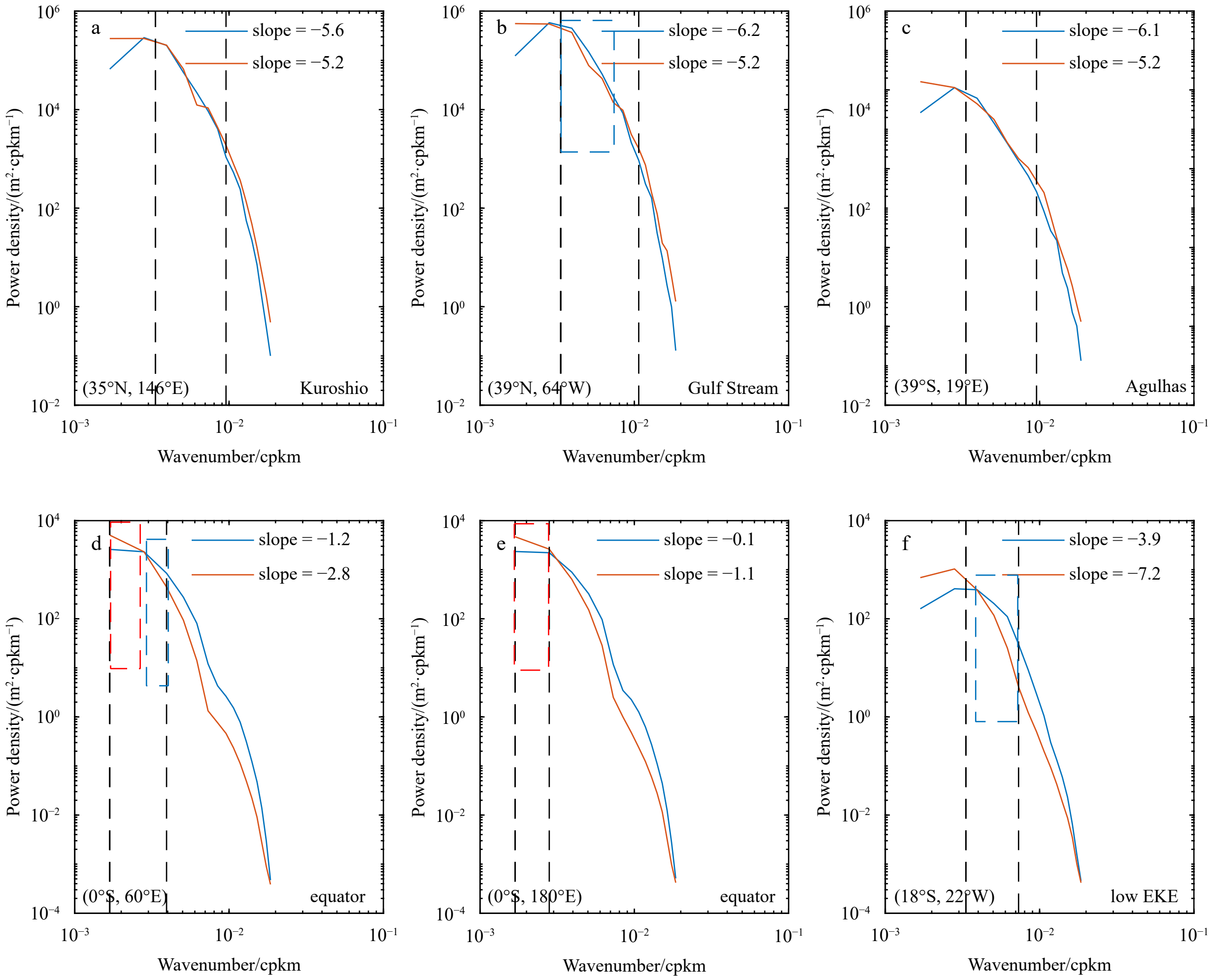

Fig. 10. Zonal (blue) and meridional (red) SSH wavenumber spectra in high-EKE regions (a, b and c), equatorial regions (d and e) and low-EKE regions (f). The black dotted lines indicate the upper and lower limit wavelengths for slope calculation. Obvious anisotropy of the inverse cascade is framed with red (the meridional power density is higher) and blue (the zonal power density is higher) dashed squares.

5.2 *Analysis of the applications of the QG and SQG theories*

Before comparison, it should be reiterated that previous spectral studies focused on the forward cascade of enstrophy, whereas this study focused on the inverse cascade of baroclinic KE. We could not compare the slope value directly because typical theories provide different slope predictions in the two inertial ranges.

Using 24 days of Seasat data, Fu (1983) suggested that the QG theory is an appropriate dynamics framework in high-EKE areas. Le Traon et al. (1990) used a much longer altimetric record (two years of Geosat data) to investigate the mesoscale variability in the North Atlantic and obtained similar results. Wang et al. (2010) calculated the KE wavenumber spectra in the GS region from ADCP measurements, which again supported the QG theory. On the contrary, recent studies based on more accurate altimeter observations concluded that the SQG theory, with a flatter SSH spectrum, is more suitable in high-EKE areas (Le Traon et al., 2008; Xu and Fu, 2011). However, Xu and Fu (2012) suggested that altimeter instrument noise correction would flatten the SSH wavenumber spectrum, such that the real slope value might be steeper than the SQG prediction.

Based on our results (Fig. 5b), however, even when compared with the QG theory predictions, the SSH spectrum is significantly steeper in high-EKE regions. This discrepancy can be attributed to the quality difference between the gridded and along-track data. The smoothing and filtering in the gridding process might reduce small-scale signals and cause a steeper spectrum, while the measurement noise of the along-track data might flatten the spectrum (Xu and Fu, 2012; Wang et al., 2019). Both of these factors could cause the gridded spectra to be steeper than the corresponding along-track results.

5.3 *Map of the SSH wavenumber spectral slopes*

The geographical distribution of the gridded SSH wavenumber spectral slopes in the inverse cascade inertial range (Fig. 5a) shares a similar spatial pattern to that of the along-track spectral slopes in the forward cascade range (Xu and Fu, 2012; Vergara et al., 2019; Wang et al., 2019). Furthermore, our map depicts clearer structures of the major currents and a more obvious relationship between the spectral slope and EKE. Moreover, the detailed differences between our results and those of previous studies (in the eastern subtropical Pacific and “eddy deserts”) are shown in Sections 3.2 and 3.3. Vergara et al. (2019) obtained results from SARAL/AltiKa with a high-value center in the eastern subtropical Pacific, which is consistent with our results. In terms of the “eddy deserts", Wang et al. (2019) showed high-value centers in the scalar spectral slope map but low-value centers in the along-track spectral slope map. Thus, the discrepancy in "eddy deserts" might result from the information mission of the along-track spectrum compared with the scalar spectrum.

5.4 *Anisotropy*

Wang et al. (2019) obtained zonal and meridional SSH wavenumber spectra using globally gridded SLA data. Compared with the meridional spectra, their zonal spectra are steeper (flatter) at low (high) latitudes, which seems to be perpendicular to but essentially consistent with our results. This apparent discrepancy is attributed to the different methods used to calculated the wavenumber spectrum. They computed zonal (meridional) SSH wavenumber spectra by averaging all the SSH spectra from the zonal (meridional) SLA as follows (Wang et al., 2019):

$$E_{\rm zonal}(kx) = {\rm fft}({\rm SSH}(x,\ y_0)), \tag{33}$$

$$E_{\rm meridional}(kx) = {\rm fft}({\rm SSH}(x_0,\ y)). \tag{34}$$

Meanwhile, from the geostrophic equation, the following equations can be obtained:

$$v = \frac{g}{f}\frac{\partial \eta}{\partial x}, \tag{35}$$

$$u = -\frac{g}{f}\frac{\partial \eta}{\partial y}. \tag{36}$$

Hence, the one-dimensional SSH wavenumber spectra that they computed are perpendicular to the KE wavenumber spectra. This paper computes the zonal (meridional) SSH spectra by summing all the 2-D spectra in a box with wavenumbers $k_x < k_y$ ($k_y < k_x$), such that they are parallel to the KE wavenumber spectra. To verify this finding, we calculated the one-dimensional spectrum using Eqs (33) and (34) and obtained similar results to those of Wang et al. (2019) (not shown here).

6 Conclusions

This study turns its attention from the forward enstrophy cascade to the inverse KE cascade. Through the spectral KE flux spectrum, the inverse KE cascade is verified to be a robust feature of most oceans, which is consistent with previous studies (Scott and Wang, 2005; Tulloch et al., 2011; Wang et al., 2015). Using 20-year gridded SLA data observed by multisatellite altimeters, the spectral characteristics of the inverse KE cascade are explored by discussing the geographic patterns of the SSH wavenumber spectral slope. The slope is calculated in a geographically variable wavelength band, which was defined following the speed-based eddy scale $L_{\rm s}$ calculated by Chelton et al. (2011), the first baroclinic Rossby radius of deformation $L_{\rm r}$ calculated by Chelton et al. (1998), and the shape of the SSH spectrum itself.

Based on our research, the results of the inverse KE cascade can be obtained. At mid-high latitude regions with high EKE, baroclinic instability occurs in the deep ocean (Tulloch et al., 2011). The QG turbulence theory is a better dynamic framework at the edges of these regions, and the inverse KE cascade in these regions tends to present a $k^{-11/3}$ power law in the SSH spectrum. In tropical regions, the β-effect is significant, resulting in baroclinic instability surface intensification (Tulloch et al., 2011). Thus, the SQG theory is a suitable dynamic, and the inverse KE cascade tends to present a k^{-3} power law in the SSH spectrum in these areas. Moreover, the QG and SQG theories do not always apply because the complex processes in the real ocean are not considered and typical oceanic velocity profile contain a mix of both surface and nonconstant interior gradients.

The correlation analysis indicates that the spectral slope and lg(EKE) are first-order linearly related with a high correlation coefficient of 0.67 at mid-latitudes. In particular, "eddy deserts" show an exactly opposite correlation, and regions with very low EKE levels ($<10^{3.2}$ m^2/s^2) show no significant correlation between the spectral slope and lg(EKE).

The anisotropic characteristics of the inverse cascade were also explored. The anisotropy is obvious in the tropics. There, mesoscale eddies are zonally stretched due to the β-effect, whereas large-scale signals are meridionally elongated due to the meridional oscillation of the predominant zonal currents. The combination of these two factors produces a steeper spectral slope at meridional scales and a higher EKE at zonal scales. In the high-EKE regions around the western boundary currents and the ACC, meridionally elongated large-scale signals do not affect the slope calculation because they exceed the inverse cascade band. Meanwhile, the zonal elongation of mesoscale eddies is not so significant that the integral EKE is higher in the meridional direction. Moreover, because of the widespread existence of anisotropic characteristics in mesoscale eddies, the along-track spectrum used by previous studies cannot reveal the dynamics of the mesoscale variabilities well, and the scalar spectrum is more suitable for this question. The dynamics of the anisotropic characteristics are beyond the scope of this study, constituting an interesting question that requires further research.

Acknowledgements

The altimeter products are created by the Data Unification and Altimeter Combination System (DUACS) and distributed by the Copernicus Marine Environment Monitoring Service (CMEMS), which can be downloaded from http://marine.copernicus.eu/. The surface current velocity data are referenced in http://apdrc.soest.hawaii.edu/. The global first baroclinic Rossby radius, calculated by Chelton et al. (1998), can be downloaded from http://www-po.coas.oregonstate.edu/. The speed-based eddy scale was obtained and downloaded from http://wombat.coas.oregonstate.edu/eddies/nc_data.html.

References

Arbic B K, Flierl G R. 2004. Baroclinically unstable geostrophic turbulence in the limits of strong and weak bottom Ekman friction: application to midocean eddies. Journal of Physical Oceanography, 34(10): 2257–2273, doi: 10.1175/1520-0485(2004)034<2257:BUGTIT>2.0.CO;2

Batchelor G K. 1969. Computation of the energy spectrum in homogeneous two-dimensional turbulence. The Physics of Fluids, 12(12): II-233–II-239

Blumen W. 1978. Uniform potential vorticity flow: part I. Theory of wave interactions and two-dimensional turbulence. Journal of the Atmospheric Sciences, 35(5): 774–783

Bourles B, Molinari R L, Johns E, et al. 1999. Upper layer currents in the western tropical North Atlantic (1989–1991). Journal of Geophysical Research: Oceans, 104(C1): 1361–1375, doi: 10.1029/1998JC900025

Charney J G. 1971. Geostrophic turbulence. Journal of the Atmospheric Sciences, 28(6): 1087–1095, doi: 10.1175/1520-0469(1971)028<1087:GT>2.0.CO;2

Chelton D B, deSzoeke R A, Schlax M G, et al. 1998. Geographical variability of the first baroclinic rossby radius of deformation. Journal of Physical Oceanography, 28(3): 433–460, doi: 10.1175/1520-0485(1998)028<0433:GVOTFB>2.0.CO;2

Chelton D B, Schlax M G, Samelson R M, et al. 2007. Global observations of large oceanic eddies. Geophysical Research Letters, 34(15): L15606

Chelton D B, Schlax M G, Samelson R M. 2011. Global observations of nonlinear mesoscale eddies. Progress in Oceanography, 91(2): 167–216, doi: 10.1016/j.pocean.2011.01.002

Eden C. 2007. Eddy length scales in the North Atlantic Ocean. Journal of Geophysical Research: Oceans, 112(C6): C06004

Ferrari R, Wunsch C. 2009. Ocean circulation kinetic energy: reservoirs, sources, and sinks. Annual Review of Fluid Mechanics, 41: 253–282, doi: 10.1146/annurev.fluid.40.111406.102139

Fu L L. 1983. On the wave number spectrum of oceanic mesoscale variability observed by the SEASAT altimeter. Journal of Geophysical Research: Oceans, 88(C7): 4331–4341, doi: 10.1029/JC088iC07p04331

Fu L L. 2004. Latitudinal and frequency characteristics of the westward propagation of large-scale oceanic variability. Journal of Physical Oceanography, 34(8): 1907–1921, doi: 10.1175/1520-0485(2004)034<1907:LAFCOT>2.0.CO;2

Galperin B, Sukoriansky S, Dikovskaya N. 2010. Geophysical flows with anisotropic turbulence and dispersive waves: flows with a β-effect. Ocean Dynamics, 60(2): 427–441, doi: 10.1007/s10236-010-0278-2

Held I M, Pierrehumbert R T, Garner S T, et al. 1995. Surface quasi-geostrophic dynamics. Journal of Fluid Mechanics, 282: 1–20, doi: 10.1017/S0022112095000012

Jacobs G A, Barron C N, Rhodes R C. 2001. Mesoscale characteristics. Journal of Geophysical Research: Oceans, 106(C9): 19581–19595, doi: 10.1029/2000JC000669

Khatri H, Sukhatme J, Kumar A, et al. 2018. Surface ocean enstrophy, kinetic energy fluxes, and spectra from satellite altimetry. Journal of Geophysical Research: Oceans, 123(5): 3875–3892, doi: 10.1029/2017JC013516

Kobashi F, Kawamura H. 2002. Seasonal variation and instability nature of the North Pacific Subtropical Countercurrent and the Hawaiian Lee Countercurrent. Journal of Geophysical Research: Oceans, 107(C11): 3185, doi: 10.1029/2001JC001225

Kraichnan R H. 1967. Inertial ranges in two-dimensional turbulence. Physics of Fluids, 10(7): 1417–1423, doi: 10.1063/1.1762301

Le Traon P Y, Klein P, Hua B L, et al. 2008. Do altimeter wavenumber spectra agree with the interior or surface quasigeostrophic theory?. Journal of Physical Oceanography, 38(5): 1137–1142, doi: 10.1175/2007JPO3806.1

Le Traon P Y, Nadal F, Ducet N. 1998. An improved mapping method of multisatellite altimeter data. Journal of Atmospheric and Oceanic Technology, 15(2): 522–534, doi: 10.1175/1520-0426(1998)015<0522:AIMMOM>2.0.CO;2

Le Traon P Y, Rouquet M C, Boissier C. 1990. Spatial scales of mesoscale variability in the North Atlantic as deduced from Geosat data. Journal of Geophysical Research: Oceans, 95(C11): 20267–20285, doi: 10.1029/JC095iC11p20267

Leith C E. 1968. Diffusion approximation for two-dimensional turbulence. The Physics of Fluids, 11(3): 671–672

Liu Zhiliang, Pang Chongguang. 2017. The Rhines effect on the geographical characteristics of altimeter-observed eddies. Acta Oceanologica Sinica, 36(9): 10–14, doi: 10.1007/s13131-017-1105-0

Montgomery D C, Peck E A, Vining G G. 2001. Introduction to Linear Regression Analysis. 3rd ed. New York: Wiley

Pascual A, Faugère Y, Larnicol G, et al. 2006. Improved description of the ocean mesoscale variability by combining four satellite altimeters. Geophysical Research Letters, 33(2): L02611

Peterson R G, Stramma L. 1991. Upper-level circulation in the South Atlantic Ocean. Progress in Oceanography, 26(1): 1–73, doi: 10.1016/0079-6611(91)90006-8

Pujol M I, Faugère Y, Taburet G, et al. 2016. DUACS DT2014: the new multi-mission altimeter data set reprocessed over 20 years. Ocean Science Discussions, 12(5): 1067–1090, doi: 10.5194/os-12-1067-2016

Qiu Bo, Chen Shuiming. 2004. Seasonal modulations in the eddy field of the South Pacific Ocean. Journal of Physical Oceanography, 34(7): 1515–1527, doi: 10.1175/1520-0485(2004)034<1515:SMITEF>2.0.CO;2

Qiu Bo, Scott R B, Chen Shuiming. 2008. Length scales of eddy generation and nonlinear evolution of the seasonally modulated South Pacific Subtropical Countercurrent. Journal of Physical Oceanography, 38(7): 1515–1528, doi: 10.1175/2007JPO3856.1

Rhines P B. 1975. Waves and turbulence on a beta-plane. Journal of Fluid Mechanics, 69(3): 417–443, doi: 10.1017/S0022112075001504

Rhines P B. 1979. Geostrophic turbulence. Annual Review of Fluid Mechanics, 11: 401–441, doi: 10.1146/annurev.fl.11.010179.002153

Salmon R. 1998. Lectures on Geophysical Fluid Dynamics. New York: Oxford University Press, 378

Scott R B, Wang Faming. 2005. Direct evidence of an oceanic inverse kinetic energy cascade from satellite altimetry. Journal of Physical Oceanography, 35(9): 1650–1666, doi: 10.1175/JPO2771.1

Smith K S. 2007. The geography of linear baroclinic instability in Earth's oceans. Journal of Marine Research, 65(5): 655–683, doi: 10.1357/002224007783649484

Spall M A. 2000. Generation of strong mesoscale eddies by weak ocean gyres. Journal of Marine Research, 58(1): 97–116, doi: 10.1357/002224000321511214

Stammer D. 1997. Global characteristics of ocean variability estimated from regional TOPEX/Poseidon altimeter measurements. Journal of Physical Oceanography, 27(8): 1743–1769, doi: 10.1175/1520-0485(1997)027<1743:GCOOVE>2.0.CO;2

Stewart R H, Shum C K, Tapley B, et al. 1996. Statistics of geostrophic turbulence in the Southern Ocean from satellite altimetry and numerical models. Physica D: Nonlinear Phenomena, 98(2–4): 599–613

Stewart K D, Spence P, Waterman S, et al. 2015. Anisotropy of eddy variability in the global ocean. Ocean Modelling, 95: 53–65, doi: 10.1016/j.ocemod.2015.09.005

Tchilibou M, Gourdeau L, Morrow R, et al. 2018. Spectral signatures of the tropical Pacific dynamics from model and altimetry: a focus on the meso-/submesoscale range. Ocean Science, 14(5): 1283–1301, doi: 10.5194/os-14-1283-2018

Theiss J. 2004. Equatorward energy cascade, critical latitude, and the predominance of cyclonic vortices in geostrophic turbulence. Journal of Physical Oceanography, 34(7): 1663–1678, doi: 10.1175/1520-0485(2004)034<1663:EECCLA>2.0.CO;2

Tulloch R, Marshall J, Hill C, et al. 2011. Scales, growth rates, and spectral fluxes of baroclinic instability in the ocean. Journal of Physical Oceanography, 41(6): 1057–1076, doi: 10.1175/2011JPO4404.1

Vallis G K. 2007. Atmospheric and Oceanic Fluid Dynamics: Fundamentals and Large-scale Circulation. Cambridge: Cambridge University Press, 770

Vallis G K, Maltrud M E. 1993. Generation of mean flows and jets on a beta plane and over topography. Journal of Physical Oceanography, 23(7): 1346–1362, doi: 10.1175/1520-0485(1993)023<1346:GOMFAJ>2.0.CO;2

Vergara O, Morrow R, Pujol I, et al. 2019. Revised global wave number spectra from recent altimeter observations. Journal of Geophysical Research: Oceans, 124(6): 3523–3537, doi: 10.1029/2018JC014844

Wang Dongping, Flagg C N, Donohue K, et al. 2010. Wavenumber spectrum in the gulf stream from shipboard ADCP observations and comparison with altimetry measurements. Journal of Physical Oceanography, 40(4): 840–844, doi: 10.1175/2009JPO4330.1

Wang Shihong, Liu Zhiliang, Pang Chongguang. 2015. Geographical distribution and anisotropy of the inverse kinetic energy cascade, and its role in the eddy equilibrium processes. Journal of Geophysical Research: Oceans, 120(7): 4891–4906, doi: 10.1002/2014JC010476

Wang Shihong, Qiao Fangli, Dai Dejun, et al. 2019. Anisotropy of the sea surface height wavenumber spectrum from altimeter observations. Scientific Reports, 9(1): 15896, doi: 10.1038/s41598-019-52328-w

Wortham IV C J L. 2013. A multi-dimensional spectral description of ocean variability with applications [dissertation]. Woods Hole: Massachusetts Institute of Technology and Woods Hole Oceanographic Institution, 184

Xu Yongsheng, Fu L L. 2011. Global variability of the wavenumber spectrum of oceanic mesoscale turbulence. Journal of Physical Oceanography, 41(4): 802–809, doi: 10.1175/2010JPO4558.1

Xu Yongsheng, Fu L L. 2012. The effects of altimeter instrument noise on the estimation of the wavenumber spectrum of sea surface height. Journal of Physical Oceanography, 42(12): 2229–2233, doi: 10.1175/JPO-D-12-0106.1

Zhou Xiaohui, Wang Dongping, Chen Dake. 2015. Global wavenumber spectrum with corrections for altimeter high-frequency noise. Journal of Physical Oceanography, 45(2): 495–503, doi: 10.1175/JPO-D-14-0144.1

Appendix A: The reason for 100-d high-pass filtering

The KE of the equatorial Atlantic and the GS were calculated using 5-a (from 1 August 1999 to 31 July 2004) surface current velocity data from SCUD (surface current from a diagnostic model) obtained from the Asia-Pacific Data Research Center/International Pacific Research Center (APDRC/IPRC). The time resolution of the raw data is 1 d, and the special resolution is (1/4)° × (1/4)°.

The power spectra of the regionally averaged KE in a 5° × 5° box was computed in the equatorial Atlantic (Fig. A1a), which represents the tropical area, and the GS (Fig. A1b), which represents the high-eddy energy area.

As shown in Fig. A1, KE has significant periods at a time scale of within half a year, mainly concentrated in the bands shorter and longer than 100 d. Waves have frequencies lower than those of eddies, especially in mid-latitude areas. Hence, confirming the former as an eddy signal and confirming the latter as a wave signal is feasible. Thus, a 100-d high-pass filter is an available method for removing wave signals.

Figure A2 shows the SSH wavenumber spectra in the same areas shown in Fig. A1, and they are estimated from data filtered by different methods. Compared with other filtering methods, the 100-d high-pass filtering can significantly reduce the signals from a large scale, representing the wave signals, and this method has little impact on small- and medium-scale signals.

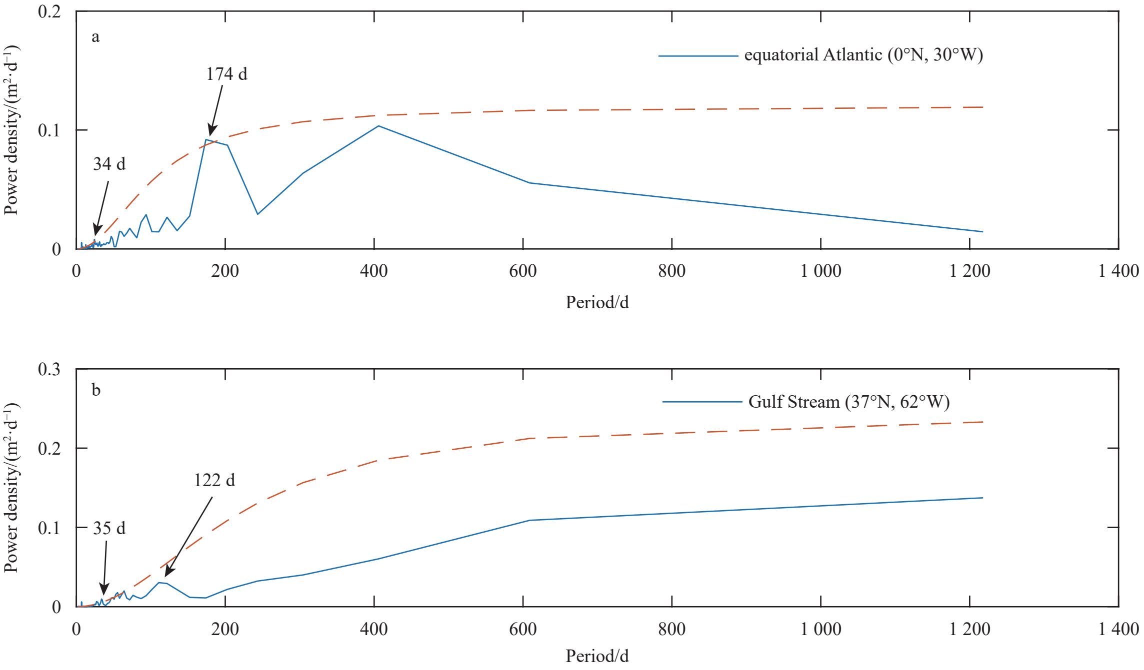

Fig. A1. The power spectra of the regionally averaged (5° × 5°) KE in the equatorial Atlantic (a) and the Gulf Stream (b).

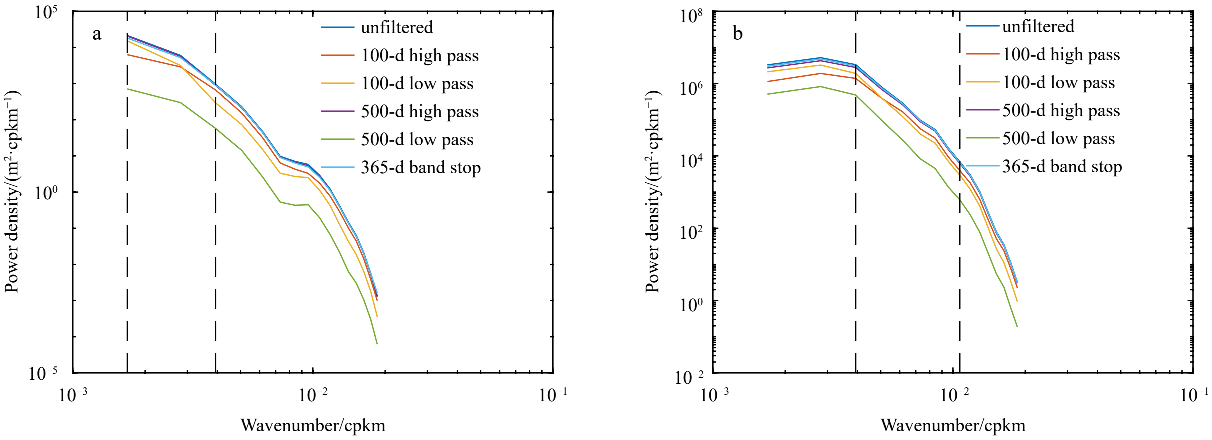

Fig. A2. Time-averaged scalar SSH wavenumber spectra at the equatorial Atlantic Ocean (a) and the Gulf Stream (b) estimated from the data filtered by different methods using 20-a gridded multisatellite measurements. The black dotted lines perpendicular to the *x*-axis indicate the upper and lower limit wavelengths, respectively.

Appendix B: Estimate of the wavenumber spectral slope error

The wavenumber spectral slope error was estimated following Xu and Fu (2011). Using the least squares fitting method within the appropriate wavenumber range, a linear equation was fitted to each averaged spectrum as follows:

$$y = \varepsilon_1 x + \varepsilon_2, \tag{B1}$$

where $y = \lg P$, $x = \lg k$, and P is the spectral power at wavenumber k. The confidence interval of the slope regression coefficient ε_1 is given by the following equation (Montgomery et al., 2001):

$$e = t_{\alpha/2,n-2} \cdot \sqrt{\frac{\sum\limits_{i=1}^{n} (\Delta y_i)^2}{\sum\limits_{i=1}^{n} (x_i - \bar{x})^2}}, \tag{B2}$$

where $t_{\alpha/2,n-2}$ is the percentile of the t distribution with α level of significance and (n–2) degrees of freedom, which is the number of data; Δy is the difference between the fitted and real values of y. In our study, n is the number of eligible points (inside the wavenumber band selected) in the spectrum. The square-root term is the standard error of the estimate of the slope regression coefficient ε_1. At the 95% confidence level, $\alpha = 0.05$. The error bar for the global ocean is shown in Fig. B1.

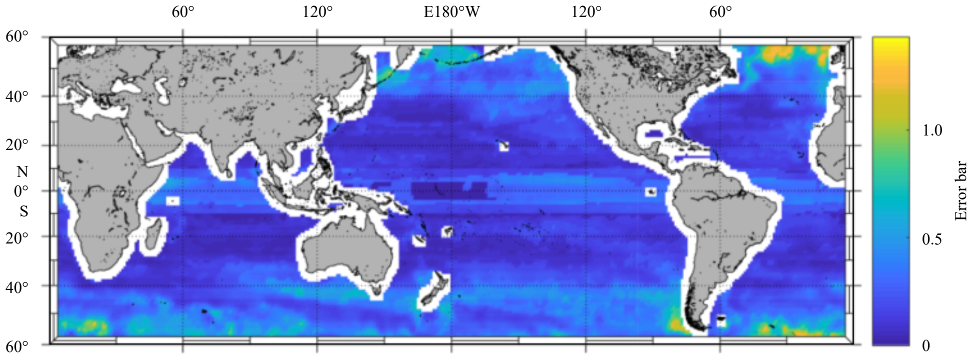

Fig. B1. The error bar at the 95% confidence level of the spectral slopes of the SSH wavenumber spectrum in the variable wavelength band estimated based on the gridded data from altimeter measurements.